Advanced Steel Construction – Vol. 21 No. 3 (2025) 218–230
DOI:10.18057/IJASC.2025.21.3.4

LOCAL BUCKLING MECHANISM OF COLD-FORMED STEEL BUILT-UP COLUMNS: EXPERIMENTAL AND NUMERICAL INVESTIGATION

Yan-Chun Li [1], Yan Lu [2], Ai-Hong Han [1], Wei-Hua Li [1], Xin-Wei Wang [1] and Zong-Liang Wu [1, *]

[1] *School of Civil Engineering And Communication, North China University of Water Resources and Electric Power, Zhengzhou 450045, China*
[2] *School of Civil Engineering Inner Mongolia University of Technology, Hohhot, Inner Mongolia, P.R.China*
** (Corresponding author: E-mail: 13523442144@163.com)*

ABSTRACT

This study aims to providing in-depth insights into the local buckling mechanisms of cold-formed steel built-up box section (CFSBBS) columns. The CFSBBS is constructed from C- and U-section components that are connected using self-drilling screws at the flanges. The investigation encompasses both experimental and numerical analyses of buckling behaviors, failure characteristics, the interaction of plates, and the ultimate bearing capacity of the columns. The dimensions of the specimens were meticulously designed to facilitate the examination of pure local buckling modes, utilizing finite strip software CUFSM and the direct strength method. A finite element model was established to perform parametric studies aimed at elucidating the impact of the built-up flange plates on the buckling performance of CFSBBS columns. Three cross-sectional types were developed to assess the effect of screw spacing on the failure modes and ultimate bearing capacities of the CFSBBS columns. The results indicate that the in-plane deformation of the C-section flanges is partially constrained by the U-section flanges. The shape of the local buckling half-wave of the C-section may change due to the interaction of buckling between the C- and U-section component. Nevertheless, the influence on the ultimate bearing capacity is relatively small, within 10%. The findings of this research will serve as a foundational basis for future investigations.

ARTICLE HISTORY

Received: 25 March 2024
Revised: 3 January 2025
Accepted: 8 January 2025

KEYWORDS

Cold-formed steel built-up box section columns;
Local buckling;
Screw spacing;
Experiment;
Numerical simulation;
Plate group effect

Copyright © 2025 by The Hong Kong Institute of Steel Construction. All rights reserved.

1. Introduction

Local buckling represents a common challenge that differentiates cold-formed steel (CFS) from hot-rolled steel sections. Notably, CFS members retain their load-bearing capacity even after experiencing local buckling, attributable to the membrane effect inherent in CFS materials. Research on local buckling has its origins in the analysis of individual thin plates, with a primary focus on assessing their stability performance at the point of branch buckling. Numerous scholars have investigated the buckling modes of CFS built-up columns [1-6]. The ultimate bearing capacity of the CFS built-up columns was studied through experiment, numerical simulation, and theory [7-9]. The influence of the mutual effect between the plates and components in the CFS built-up members was not ignored [10,11]. However, few scholars analyze this key factor from the instability mechanism.

The majority of research concerning local buckling has primarily concentrated on individual thin plates, with analyses focusing on stability at the bifurcation point. Timoshenko [12] conducted a comprehensive investigation into the critical buckling load (CBL) of plates subjected to various boundary conditions and loading scenarios. Nonetheless, it is important to note that the plates within an actual cross-section are not independent entities. The plates constituting compression members exert a mutual constraint during local buckling, a phenomenon referred to as the "plate group effect" [13]. This effect serves to restrict the initial buckling of certain plates, ultimately leading to simultaneous buckling across all plates. To account for this interaction, a theoretical formula was proposed for calculating the local CBL of compressed members, incorporating the "plate group effect" [14]. Szymczak and Kujawa [14] further explored the theoretical aspects of the local CBL in simply supported channel steel, emphasizing the significance of the "plate group effect" [15,16]. CFS built-up box-section columns, which are comprised of multiple plates, also experience this mutual constraint, thereby influencing their buckling modes and ultimate strength. The buckling modes and the ultimate strength of CFS built-up columns will be affected by this factor. Consequently, it is imperative to consider the stability of the individual panels when designing such columns. However, there exists a paucity of research addressing the "plate group effect" specifically in the context of CFS built-up columns.

Several studies have examined the behavior of CFS built-up columns, primarily emphasizing the effects of geometric dimensions, screw spacing, screw arrangement, and cross-sectional types on the load-bearing capacity of these columns [17-20]. Fratamico [21] conducted experimental investigations into the buckling and failure behavior of composite columns, quantifying the ultimate strength, built-up actions, buckling interactions, and collapse behaviors of CFS built-up members. Kherbouche [5] performed both experimental and numerical analyses to assess the ultimate strength, deformation patterns, and lateral displacements of CFS closed-section columns, while also evaluating the impact of the thickness of the built-up components on bearing capacity and proposing a calculation method based on the direct strength approach. Chen [22] explored CFS back-to-back built-up columns with varying cross-sectional types, analyzing how the form of stiffening and the dimensions of web openings affect the bearing capacity of the CFS built-up columns. The majority of research concerning screw spacing has concentrated on the bearing capacity and failure modes of CFS built-up members [19-23]. Comprehensive investigations into the influence of screw spacing on the interaction between assembled plates are limited. Existing research indicates that the assembly effect does not enhance the ultimate capacity of CFS built-up box sections or built-up I-section members that are subjected to local buckling. Members characterized by partially built-up sections are prone to distortional buckling in the open component and local buckling in the closed component. Consequently, the relationship between various buckling modes and the ultimate capacity of built-up members is intricate [24-28]. Most studies yield only qualitative findings, which lack consistency. Both experimental and theoretical analyses have been performed to assess the mechanical performance and load-bearing capacity of CFS columns across different built-up configurations [29-33]. Lu [34] conducted a theoretical examination of the bearing capacity of CFS C-section columns subjected to local buckling and subsequently proposed a method for calculating this capacity. However, a systematic approach to adequately account for the "plate group effect" within the effective width method (EWM) remains unresolved.

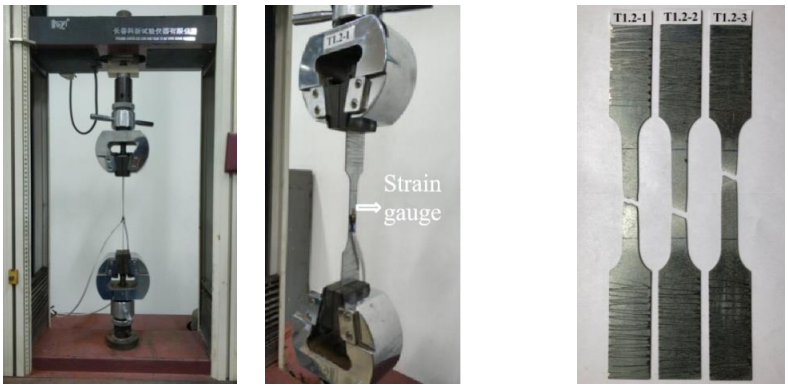
This study presents an experimental and numerical investigation into the local buckling mechanisms and ultimate load-bearing capacity of CFSBBS columns. The research examines the effects of various factors on the buckling mode and overall bearing capacity of the built-up columns. A precise finite element model was developed and validated against experimental data to facilitate subsequent finite element parameter analyses. The findings of this research offer valuable insights for the design of cross-sectional dimensions of CFSBBS columns and establish a foundational basis for future investigations.

2. Experiment

2.1. Material properties

The experimental specimen utilized in this study was composed of the CFS galvanized steel plate, specifically of steel grade S280, sourced from the web of a CFS column from the same production batch, with a thickness of 1.2 mm. All tensile testing of the steel was performed based on the standard (GB/T228.1-2010) for tensile testing of materials. The apparatus employed for

material property testing is illustrated in Fig. 1. The experimental setup incorporates a displacement-controlled loading system, operating at a loading rate of 1.5 mm/min. The testing machine autonomously manages the loading procedure and systematically records pertinent data throughout the duration of the test. A strain gauge, as depicted in Fig. 1(a), is affixed to both the front and back sides of the specimen at the midpoint of the original gauge length. Data collection is facilitated by the DH3820 high-speed static strain testing and analysis system. The outcomes of the material properties assessment are listed in Table 1.



(a) Tensile testing device (b) Testing specimen

Fig. 1 Material properties test

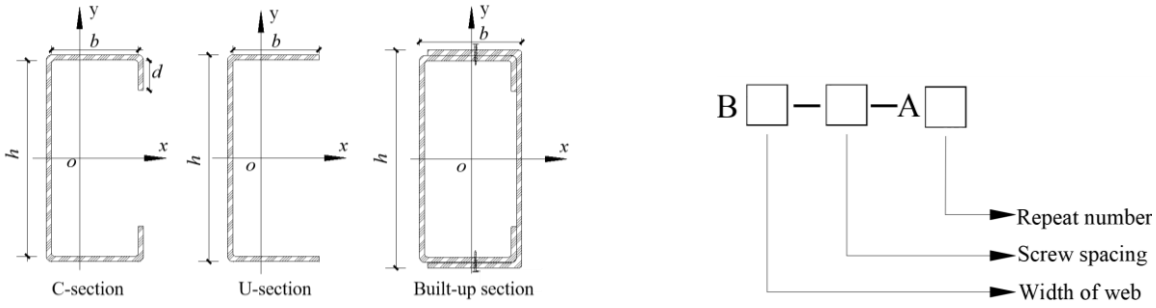
Table 1
Results of the material properties test

Specimens	Yield stress(N/mm^2)		Ultimate stress(N/mm^2)		Elastic modulus(10^5N/mm^2)		Elongation(%)	
	f_y	Mean	f_u	Mean	E	Mean	δ	Mean
T1.2-1	295.53		344.53		1.959		45	
T1.2-2	293.28	292.95	348.02	345.53	1.915	1.939	44	45.33
T1.2-3	290.04		344.05		1.943		47	

2.2. Experimental specimens

2.2.1. Section design of specimens

Three distinct types of cross-sectional members were subjected to testing, specifically C-section, U-section, and built-up box-section, as illustrated in Fig. 2(a). The local CBL (P_{crL}) and the distortional CBL (P_{crD}) for each specimen were calculated utilizing the CUFSM software [35], ensuring that the columns experienced buckling and failure in a purely local mode. The dimensions of the cross-section must satisfy the conditions $P_{crL}<0.5P_{crD}$ and $P_{uL}<P_{crD}$, where P_{uL} represents the ultimate capacity of local buckling determined through the DSM [36]. To further confirm that the designed specimens would undergo pure local buckling, finite element analysis was conducted using ABAQUS software. The nomenclature for the specimens is detailed in Fig. 2(b). For example, in B120-45-A1, The letter B represents built-up; the number 120 indicates the height of the web; the second number 45 refers to the screw spacing; the letter A represents axial compression; the last number 1 represents the number of repeated specimens.

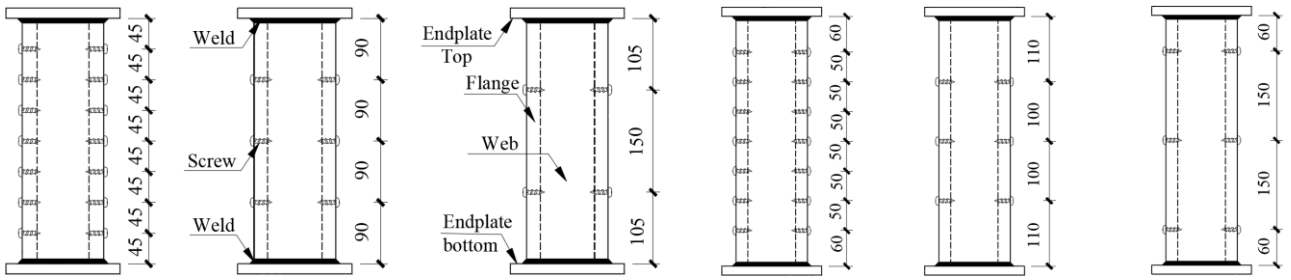


(a) Section type of test specimens (b) Naming of test pieces

Fig. 2 Overview of test piece

The CFSBBS column was assembled using ST4.8 self-drilling screws, which were strategically positioned at the center of the flanges. The half-wavelength of the specimen obtained by the software CUFSM was used as the design basis for the length of specimens and the screw spacing. According to the height of the web, two types specimens of 120 series and 140 series were studied in this paper. The local buckling half-wavelengths of 120 series and 140 series specimens obtained from CUFSM were 89.9mm and 104.2mm, respectively. The specimen is subjected to fixed-end boundary conditions at both extremities. The specimen's length was approximately three times greater than the height of the web as advised by the Structural Stability Research Council (SSRC) [37]. Consequently, the lengths of the test specimens are 360 mm and 420 mm, respectively. Furthermore, the arrangement of the screws was established based on the buckling half-wavelengths, which include measurements of 45 mm, 90 mm, 150 mm, as well as 50 mm, 100 mm, and 150 mm, respectively, as illustrated in Fig. 3.

In Fig. 2(a), the variables h, b, and d denote the height of web, the width of flange, and the length of lip, respectively. The variable t signifies the thickness of the plate, while R indicates the outer radius of the bending angle. The actual cross-sectional dimensions of all specimens, as detailed in Table 2, have been measured to accurately reflect the real conditions.



(a) B120 series column (L=360mm) (b) B140 series column (L=420mm)

Fig. 3 Layout of self-drilling screw spacing (unit: mm)

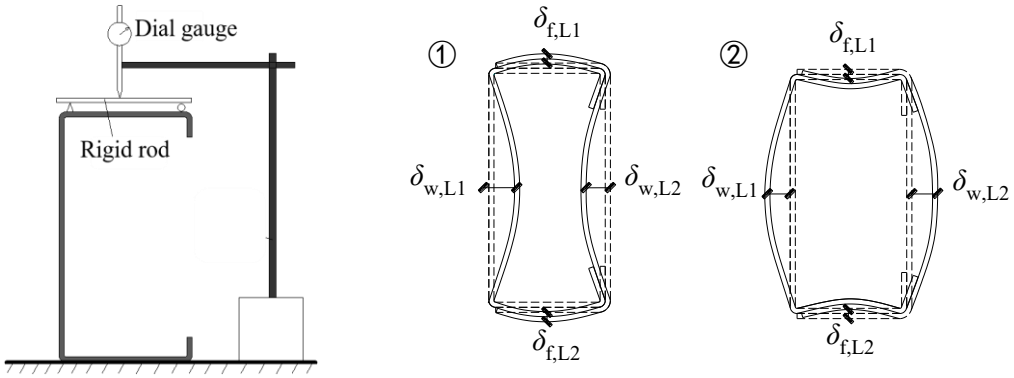
Table 2
Measured dimensions of the CFS built-up box-section column (unit: mm)

Specimens	Part	L	h	b_1	b_2	d_1	d_2	t	R	P_t/kN	P_{FE}/kN	P_{FE}/P_t
B120-45-A1	a	361	113.0	45.5	46.0	12.5	15.0	1.16	4.0	92.05	100.93	1.096
	b		117.0	49.0	48.0	\	\	1.17	3.5			
B120-45-A2	a	364	114.5	46.0	45.0	13.0	16.5	1.17	3.8	91.04	97.70	1.073
	b		116.0	47.5	50.0	\	\	1.16	3.5			
B120-45-A3	a	365	116.5	47.0	46.0	12.0	13.5	1.16	2.8	86.93	94.95	1.092
	b		118.0	49.0	47.0	\	\	1.14	3.0			
B120-90-A1	a	350	115.0	45.0	47.0	11.5	12.5	1.18	3.5	92.02	100.25	1.089
	b		116.0	48.0	51.0	\	\	1.17	3.5			
B120-90-A2	a	360	115.0	46.5	44.5	12.5	14.0	1.16	3.5	89.85	98.24	1.093
	b		118.0	50.0	47.0	\	\	1.16	3.0			
B120-90-A3	a	365	115.0	47.5	46.5	13.5	12.0	1.18	4.0	94.84	100.10	1.055
	b		118.0	46.5	50.0	\	\	1.17	2.8			
B120-150-A1	a	362	115.5	45.5	45.0	13.0	12.5	1.16	3.8	97.18	99.35	1.022
	b		118.0	47.5	50.5	\	\	1.14	3.5			
B120-150-A2	a	363	115.5	46.0	46.0	16.5	13.0	1.14	3.3	86.61	95.29	1.100
	b		118.0	47.5	49.0	\	\	1.16	3.0			
B120-150-A3	a	362	114.5	46.0	46.5	14.5	12.5	1.17	3.3	89.03	97.37	1.094
	b		113.0	45.5	46.0	12.5	15.0	1.16	4.0			
B140-50-A1	a	420	136.5	45.0	46.0	21.0	17.5	1.17	2.8	95.63	98.85	1.034
	b		137.0	47.0	47.0	/	/	1.16	4.0			
B140-50-A2	a	421	138.0	46.5	47.0	21.0	17.0	1.17	3.8	93.74	98.70	1.053
	b		139.0	45.5	47.0	/	/	1.16	3.5			
B140-50-A3	a	422	135.0	47.0	45.5	20.5	17.5	1.17	3.0	86.61	88.66	1.024
	b		138.0	46.5	47.0	/	/	1.14	3.5			
B140-100-A1	a	421	135.0	45.5	45.5	16.5	20.0	1.15	3.5	88.28	95.47	1.081
	b		136.0	46.5	48.0	/	/	1.16	4.5			
B140-100-A2	a	420	135.0	41.0	46.5	21.0	17.0	1.21	3.5	93.09	102.26	1.099
	b		138.0	46.5	47.0	/	/	1.18	3.5			
B140-100-A3	a	420	135.0	44.5	45.0	17.0	20.0	1.17	3.8	95.77	104.84	1.095
	b		137.5	47.5	47.5	/	/	1.15	3.8			
B140-150-A1	a	420	136.0	44.0	45.0	21.5	16.5	1.17	3.0	91.98	98.74	1.073
	b		137.0	45.5	50.0	/	/	1.16	4.0			
B140-150-A2	a	415	134.5	45.0	44.5	17.0	18.5	1.15	3.5	95.82	101.17	1.056
	b		138.0	45.0	47.0	/	/	1.15	3.8			
B140-150-A3	a	420	135.0	45.5	46.0	17.0	20.5	1.17	3.5	103.40	105.61	1.021
	b		137.5	47.5	46.0	/	/	1.17	3.8			
Mean												1.069
SD												0.028

2.2.2. Initial geometrical imperfection

The buckling mode and load-bearing capacity of CFS members are influenced by initial geometric imperfections. Consequently, it is essential to assess the initial geometric imperfections of the specimen prior to applying any

load. The procedure commenced with the placement of the specimen on a measuring platform, followed by the positioning of a rigid rod on a designated plate. A measurement was then obtained using a dial gauge (refer to Fig. 4(a)), after which the rigid rod was removed to facilitate the measurement of an additional value. The dial gauge utilized has a measurement range of 50 mm and an accuracy of 0.01 mm. The difference between the two recorded values represents the unflatness of the plate. The symbols denoting the measured locations and imperfection parameters are depicted in Fig. 4(b). The results of the measurements are presented in Table 3. $\delta_{w,L1}/t$, $\delta_{w,L2}/t$, $\delta_{f,L1}/t$, $\delta_{f,L2}/t$ represent the ratio of local initial imperfection to the thickness of the specimen. The maximum values of $\delta_{w,L1}/t$, $\delta_{w,L2}/t$, $\delta_{f,L1}/t$, $\delta_{f,L2}/t$ are 0.417, 0.500, 0.500, 0.333, respectively, as shown in Table 3. The data indicate that the initial geometric imperfections for these specimens are minimal, thereby satisfying the quality standards for steel structure construction.



(a) Initial imperfection device (b) Imperfection parameter symbols

Fig. 4 Initial imperfection measurement

Table 3
Initial imperfection of the CFS built-up box-section column

Specimens	t/mm	Bending/mm（Concave+，convex-）				$\delta_{w,L1}/t$	$\delta_{w,L2}/t$	$\delta_{f,L1}/t$	$\delta_{f,L2}/t$
		Web of C-section($\delta_{w,L1}$)	Web of U-section($\delta_{w,L2}$)	Left flange($\delta_{f,L1}$)	Right flange($\delta_{f,L2}$)				
B120-45-A1	1.2	0.5	0.4	0.2	0.3	0.417	0.333	0.167	0.250
B120-45-A2	1.2	0.3	0.6	0.2	0.2	0.250	0.500	0.167	0.167
B120-45-A3	1.2	0.2	0.3	0.1	0.3	0.167	0.250	0.083	0.250
B120-90-A1	1.2	0.2	0.3	0	0.3	0.167	0.250	0.000	0.250
B120-90-A2	1.2	-0.1	-0.6	-0.4	-0.3	-0.083	-0.500	-0.333	-0.250
B120-90-A3	1.2	0.3	0.4	0.5	0.2	0.250	0.333	0.417	0.167
B120-150-A1	1.2	0.5	0.3	0.3	0.3	0.417	0.250	0.250	0.250
B120-150-A2	1.2	0.5	0.4	0.6	0.3	0.417	0.333	0.500	0.250
B120-150-A3	1.2	0.5	0.4	0.2	0.3	0.417	0.333	0.167	0.250
B140-50-A1	1.2	0.3	0.4	0.5	0.3	0.250	0.333	0.417	0.250
B140-50-A2	1.2	0.4	0.2	0.2	0.4	0.333	0.167	0.167	0.333
B140-50-A3	1.2	0.2	0.5	0.2	0.4	0.167	0.417	0.167	0.333
B140-100-A1	1.2	0.3	0.5	0.2	0.3	0.250	0.417	0.167	0.250
B140-100-A2	1.2	0.5	0.4	0.3	0.4	0.417	0.333	0.250	0.333
B140-100-A3	1.2	0.3	0.5	0.6	0.3	0.250	0.417	0.500	0.250
B140-150-A1	1.2	0.3	0.6	0.6	0.3	0.250	0.500	0.500	0.250
B120-90-A3	1.2	0.3	0.4	0.5	0.2	0.250	0.333	0.417	0.167
B120-150-A1	1.2	0.5	0.3	0.3	0.3	0.417	0.250	0.250	0.250
B120-150-A2	1.2	0.5	0.4	0.6	0.3	0.417	0.333	0.500	0.250
B120-150-A3	1.2	0.5	0.4	0.2	0.3	0.417	0.333	0.167	0.250
B140-50-A1	1.2	0.3	0.4	0.5	0.3	0.250	0.333	0.417	0.250
B140-50-A2	1.2	0.4	0.2	0.2	0.4	0.333	0.167	0.167	0.333
B140-50-A3	1.2	0.2	0.5	0.2	0.4	0.167	0.417	0.167	0.333
B140-100-A1	1.2	0.3	0.5	0.3	0.3	0.250	0.417	0.250	0.250
B140-100-A2	1.2	0.4	0.4	0.3	0.4	0.333	0.333	0.250	0.333
B140-100-A3	1.2	0.3	0.5	0.6	0.3	0.250	0.417	0.500	0.250
B140-150-A1	1.2	0.3	0.6	0.6	0.3	0.250	0.500	0.500	0.250
B140-150-A2	1.2	0.3	0.3	0.4	0.1	0.250	0.250	0.333	0.083
B140-150-A3	1.2	0.2	0.3	0.2	0.2	0.167	0.250	0.167	0.167
MAX						0.417	0.500	0.500	0.333

2.3. Loading preparation

The specimen undergoes axial compressive loading via a testing apparatus, as illustrated in Fig. 5. The CFSBBS column was constructed with an end plate measuring 360 mm × 280 mm × 16 mm, which was secured using fillet welds. Subsequently, the assembly was positioned on the apparatus depicted in Fig. 5 to establish the boundary conditions necessary for a fixed joint at both ends of the column.

In this study, strain gauges and Linear Variable Differential Transformers (LVDTs) were strategically positioned on all test specimens to facilitate precise measurements of strain and displacement variations during the loading process. Furthermore, strain gauges were installed at corresponding locations both internally and externally at the same cross-sectional position to assess the CBL of the specimens, as depicted in Fig. 6. Specifically, strain gauges were placed at one-quarter, mid-point, and three-quarters along the length of the column to effectively capture the peaks and troughs of the buckling wave. Initially, a vertical alignment instrument was employed to ensure geometric alignment of the specimen post-installation. Following this, a preload of 1 kN was applied to monitor strain value changes at the symmetrical measurement points of the specimen, thereby achieving physical alignment. Upon completion of both geometric and physical alignment, formal loading commenced, with an initial loading amplitude set at 5% of the estimated ultimate load for each loading increment. Once 80% of the estimated ultimate load was attained, the loading amplitude for subsequent increments was adjusted to 2% of the estimated ultimate load.

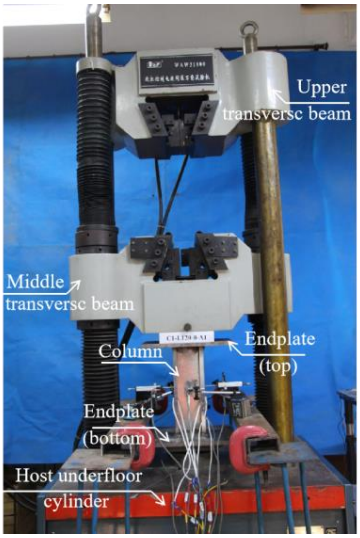


Fig. 5 Test loading device

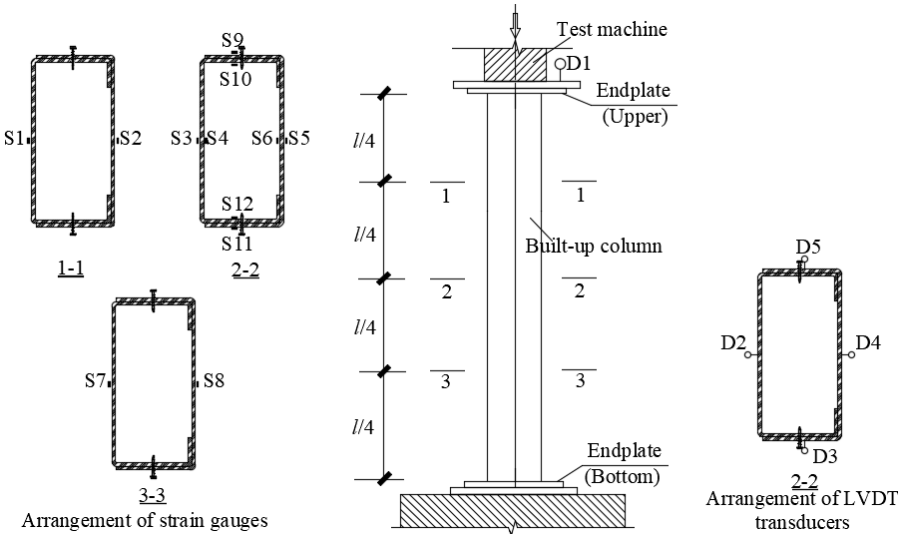


Fig. 6 Arrangement of strain gauges and LVDT transducers

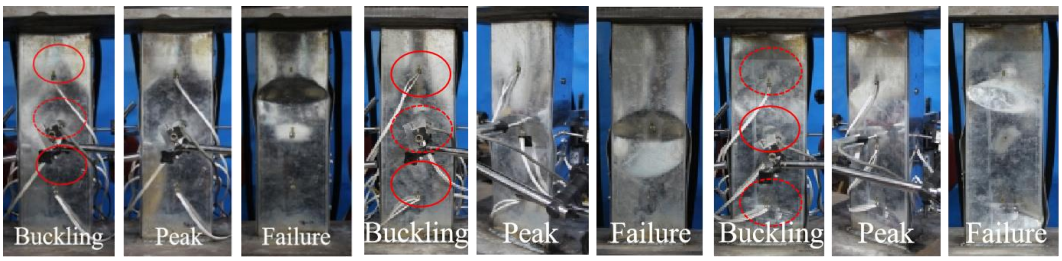
2.4. Experimental results and discussion

2.4.1. Buckling behaviors of test members

Figs 7~8 show the buckling behaviors of B120 and B140 series built-up columns. The local buckling occurred first in Figs 7~8(Buckling) as the compression load increased, regardless of the specimen section types. As the idea of designing the specimen, there are three local buckling half waves in the experimental phenomenon. It can be observed that the specimens with screw spacing of 45 mm and 50 mm appear convex-concave-convex waves from the top to the bottom of the column. While the phenomena of the concave-convex-concave waves appear on the specimens with 90 mm, 100 mm, and 150 mm screw spacing.

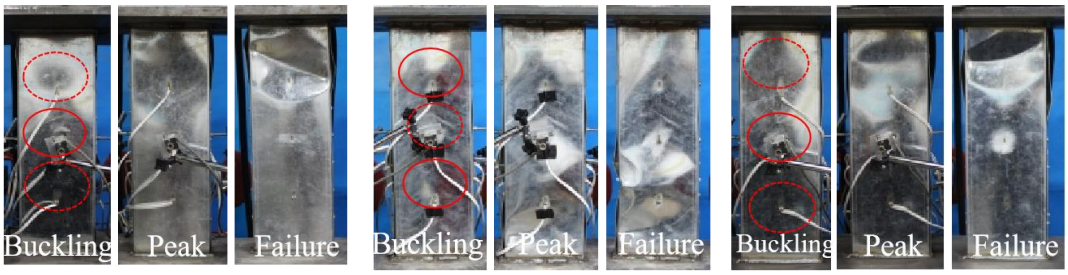
As can be seen in Figs 7~8(Buckling), the U-section part buckled locally with the flange outwards, while the corresponding C-section part buckled locally with peaks and valleys from top to bottom on its web. It should be pointed out that the inward deformation of the U-section part can not be overserved for all the investigated members. The reason for such a phenomenon can be ascribed to the built-up interaction effect, i.e., the existing C-section part constrains the corresponding U-section part's flange inwards deformation while its flange can deform outwards freely. Additionally, for the specimens whose failure positions are close to the end plate, it is mainly caused by artificial welding errors or initial defects, but the load-bearing capacity of the three specimens is basically the same.

Nonetheless, given that the constructed members exhibit a consistent reserve of strength following local buckling, the column remains capable of supporting the additional compressive load. As the load continues to escalate, the out-of-plane deformation resulting from local buckling becomes markedly pronounced, as illustrated in Fig. 7~8(Peak). Ultimately, it was observed that columns failed in the local buckling mode Figs. 7~8(Failure). Similarly with the buckling occurring stage in Figs 7~8(Buckling), all the investigated members in the failed stage with their web buckled inwards and flange buckled outwards, i.e., the built-up interaction effect also exists in the post-local-buckling bearing stage. As a result, the existence of a built-up interaction effect makes the local buckling deformation mechanism of such built-up members different from that of the single limb member.



(a) B120-45 (b) B120-90 (c) B120-150

Fig. 7 Buckling mode and failure characteristic of B120 series specimens

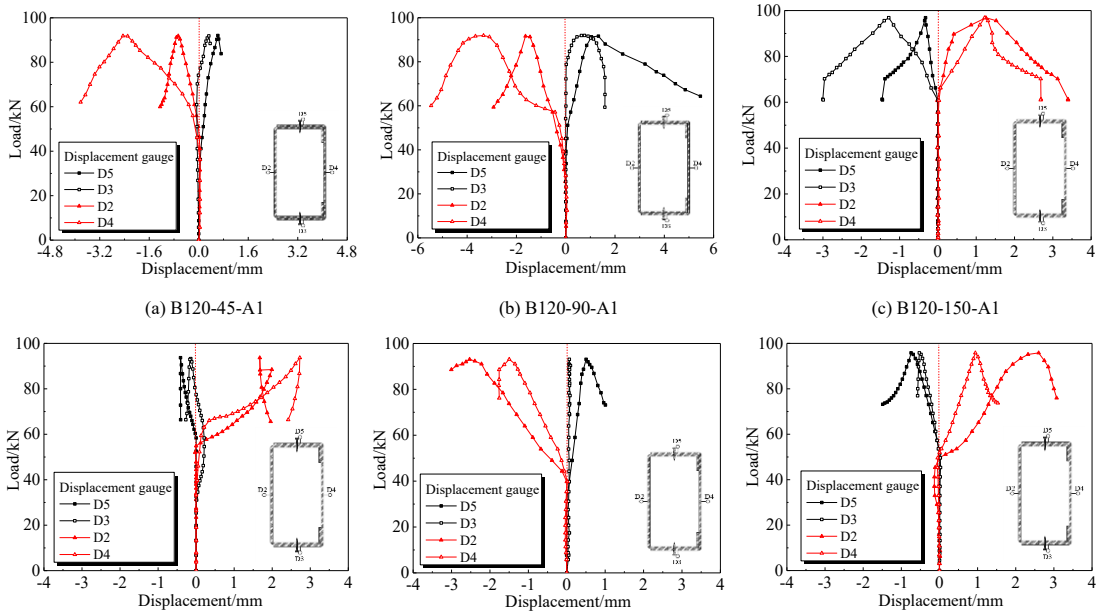


(a) B140-50 (b) B140-100 (c) B140-150

Fig. 8 Buckling mode and failure characteristic of B140 specimens

2.4.2. lateral deflection

The lateral deflection of the specimen provides a more precise representation of the specimen's buckling throughout the loading process. The lateral deflection & load-bearing capacity curves of the webs and flanges were illustrated in Fig. 9. The displacement gauges D3 and D5, positioned on the flanges of specimens B120-45-A1 and B120-90-A1, yield positive values, while gauge D2 on the web of the U-section and gauge D4 on the web of the C-section produce negative values. This indicates that the flanges of the U-section at the mid-span location are experiencing outward buckling, whereas the webs are undergoing inward buckling, which aligns with the observed experimental phenomena. Conversely, for specimens C4-L120-150-A1 and C4-L140-150-A1, the displacement gauges D3 and D5 register negative values, while D2 and D4 yield positive values. This suggests that the flanges of the U-section at the mid-span location are buckling inward, while the webs are buckling outward, a pattern that is similarly observed in the C-section. This behavior is consistent with the experimental findings. Notably, for specimen B140-50-A1, the flanges exhibit outward buckling during the initial buckling phase; however, upon reaching the load-bearing capacity, the flanges ultimately attempt to buckle inward. This behavior may be attributed to the post-buckling strength inherent in the specimen, which contributes to re-stability. Fig. 9(e) indicates that the displacement recorded by gauge D3 is 0, which may be attributed to a failure of the displacement gauge D3.



(a) B120-45-A1 (b) B120-90-A1 (c) B120-150-A1

(d) B140-50-A1 (e) B140-100-A1 (f) B140-150-A1

Fig. 9 Load-deflection curve of the built-up columns

2.4.3. Buckling pattern

The possible local buckling modes of CFS built-up box section columns under axial pressure can be predicted from the experimental phenomena. Generally, webs and flanges buckle inward and buckle outward for single-limb members (see Fig.10(a)-10(b)). The two flanges must be symmetrically outward to ensure the 90-degree angle corner if the web buckles inward, as presented in Fig.10(a) and Fig.10(b). However, such local buckling phenomena will not be uniform for CFS built-up specimens, especially for CFS built-up columns with different screw spacing. The possible local buckling modes of the CFSBBS columns by the experimental investigation are presented in Fig.10(c-f). (i) Two types of local buckling modes in the flanges between the screws are defined: ① web buckling outward and the flanges will buckle inward (see Fig.10(c)); ② web buckling inward and the flanges will buckle outward (see Fig.10(d)). It is worth noting that the deformation of the built-up flanges is coordinated buckling (the degree and direction of the out-of-plane deflection of the two single plates are basically the same) whether it is buckling inward or buckling outward. The results indicate that the C-section has a coordinated and supportive effect on the deformation of the U-section. (ii) Fig.10(e) presents the buckling modes of the built-up section close to the screw position. The two flanges of the C-section buckle outward and the web tries to buckle inward. The two flanges of the U-section buckle outward and the web is slightly buckling inward, due to the coordination effects. It is worth mentioning that the two flanges are attached together that the distance from the screw to the intersection line between the flange and the web of the U-section (see Fig.10(e)). It indicates that the constraint effect of screws. (iii) The local buckling modes of the built-up section away from the screw position are shown in Fig.10(f). The two flanges of the C-section buckle inward and the web try to buckle inward. The two flanges of the U-section buckle inward and the web is slightly buckling outward, due to the coordination effects. (iv) Someone may feel that the C-section and U-section flanges in the CFS built-up box section will be tightly bonded together at the screw position. However, the experimental phenomena show that this is not the case (see Fig.10(g)). There is only one type of local buckling mode for the two flanges of the C-section, that is, webs buckling inward and flanges try to buckle outward. This is due to the effect of the screw thread on its drawing, so that the buckling modes of webs buckling outward and flanges buckling inward cannot appear. It should be noted that the test showed that the screw would tilt, but it was not pulled out and cut. This also shows that the shear slip occurs in the built-up flange plates. From the mechanical point of view, the axial pressure will produce a lateral force when the column is buckling. Due to the screw tilting, it is impossible to

effectively resist this part of the new lateral force, which makes the local force of the member nonuniform, and may produce stress concentration in some parts. It accelerates the material to enter the yield stage and reduces the load-bearing capacity of the column.

It can be seen that the buckling mode of the U-section is affected and determined by that of the C-section. The mechanism of local buckling instability of the CFSBBS column is revealed, which further shows that the cooperative working performance of the built-up members is better and is conducive to the stability of the structure.

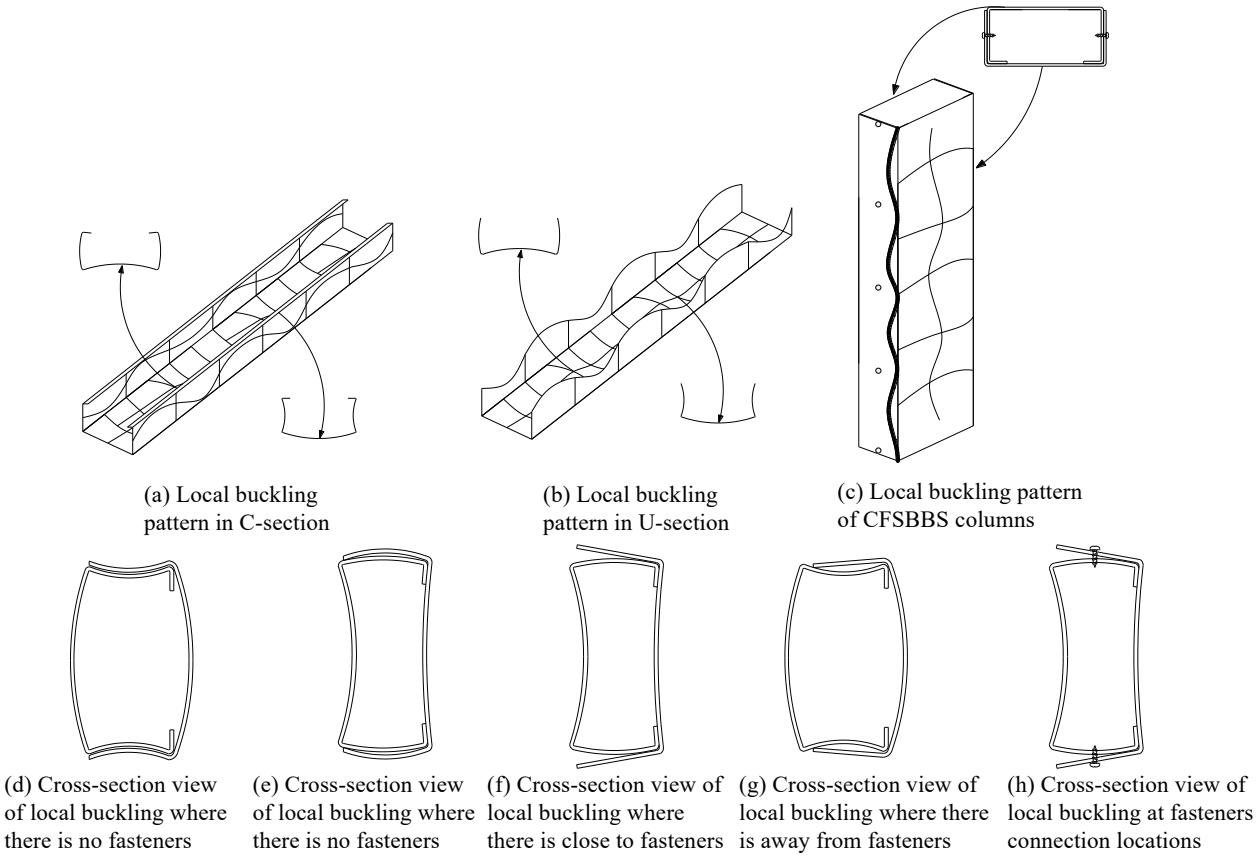


Fig. 10 Possible local buckling failure modes in CFSBBS columns

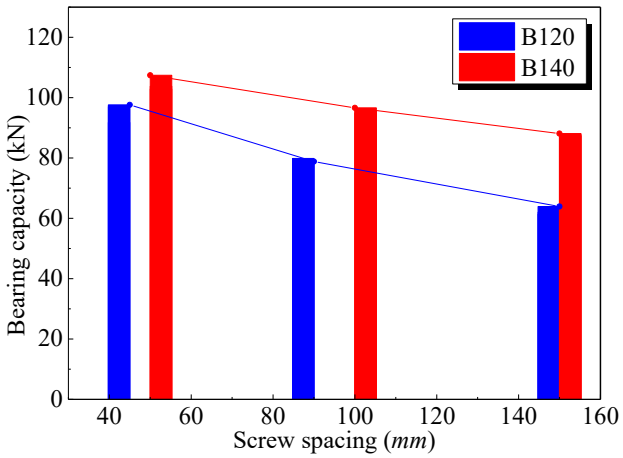


Fig. 11 Bearing capacity distribution of B120 and B140 members

2.4.4. Ultimate bearing capacity

The test results pertaining to the load-bearing capacity of the CFSBBS columns are presented in Table 2 and Fig. 11. The following key conclusions can be drawn from the analysis:

(1) The CBL and load-bearing capacity of CFSBBS are influenced by the spacing of the screws. Specifically, an increase in screw spacing correlates with a decrease in ultimate bearing capacity, suggesting that the effectiveness of the built-up section diminishes as screw spacing increases.

(2) For B120 series specimens, the variation in ultimate capacity due to different screw spacings ranges from 3% to 8%. Conversely, for the B140 series specimens, this variation is observed to be between 3% and 13%.

(3) The load-bearing capacity of specimens with a web height of 140 exceeds that of those with a web height of 120. Additionally, the B120 series specimens exhibit a greater sensitivity to changes in the screw spacing compared to the B140 series specimens.

3. Numerical simulation

The finite element (FE) software ABAQUS [38] was used to develop the linear and nonlinear numerical models of the CFSBBS columns, as illustrated in Fig.12. The geometric dimensions, initial imperfection, and material properties of FE models were all based on experimental data. The critical buckling load, elastic buckling state, failure characteristics, and the relationship between ultimate bearing capacity and axial displacement of the test specimens are obtained. The verified FE model also lays the foundation for the subsequent analysis of a large number of parameters.

3.1. Element and mesh

The finite element (FE) model utilized the S4R shell element, characterized as a four-node linear reduced integration element. Each node within this element possesses six degrees of freedom, encompassing translations along the x, y, and z axes, as well as rotations about these axes, as illustrated in Fig.12. For the modeling of the self-drilling screw ST4.8, an 8-node hexahedral linear reduced integration solid element, designated as C3D8R, was employed.

The mesh division of the FE model has two objectives: creating a sufficiently fine mesh to simulate the basic features of the deformation, and minimizing the number of elements to reduce the computational time. It is worth mentioning that the flange section of the built-up column is a perforated section with a hole in the middle, as provided in Fig.12. Therefore, the built-up flange section was divided into several regions. The 'Free Grid' command was applied to the screw area for fine meshing. A fine mesh was created near the screw hole to interpret the stress concentration. The maximum size of the shell element was 5 mm×5 mm. The mesh size of the self-drilling screw was about 0.68 mm×0.68 mm.

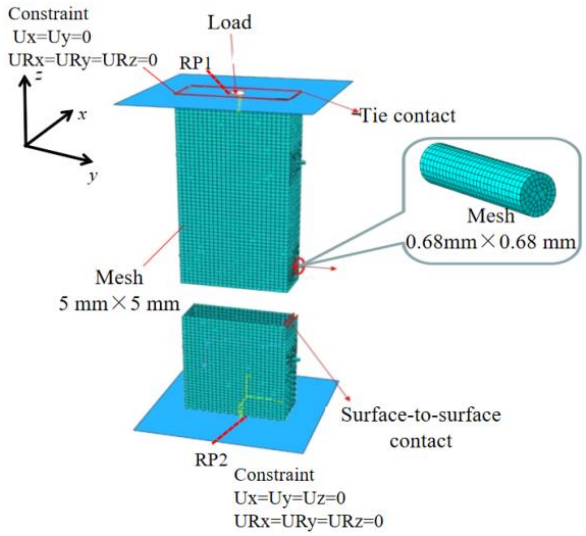


Fig. 12 Finite element model

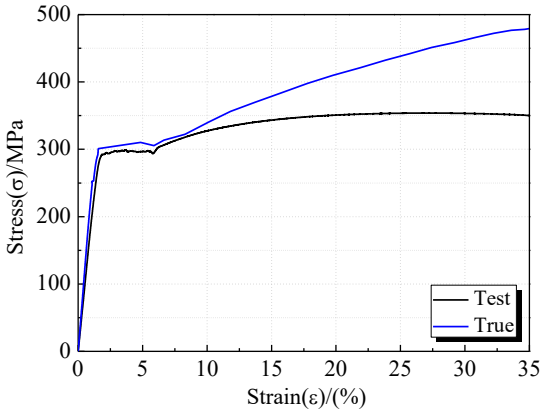


Fig. 13 Stress vs strain curve of the CFS

3.2. Material properties

The material properties of the FE models were entirely derived from the experimental results. It is important to note that there exists a discrepancy between the engineering stress-strain curve obtained from the tensile testing of the material and the actual stress-strain behavior of the material. Consequently, the measured engineering stress (σ) and strain (ε) curve was converted into the true stress ($\sigma_{true}=\sigma(1+\varepsilon)$) and strain ($\varepsilon_{true}=\ln(1+\varepsilon)-\sigma_{true}/E$) curve of the steel in accordance with the specifications of ABAQUS software. The true stress-strain curve for the CFS, as obtained through this conversion, is illustrated in Fig. 13.

3.3. Initial imperfections

CFS inevitably has certain imperfections in processing and manufacturing as other types of metal materials. These imperfections mainly include geometric imperfections and material imperfections of members. Schafer [39] proposed several modeling methods when accurate data of geometric imperfection distribution cannot be obtained. The initial imperfections may be integrated into the numerical model through the superposition of various buckling modes, with their magnitudes regulated via Fourier transformation. Schafer [39] proposed the application of a maximum deviation, roughly equivalent to the thickness of the plate, as a straightforward heuristic. In the present study, the initial eigenvalue buckling analysis of the ideal member was conducted utilizing ABAQUS software to investigate the potential buckling modes. The initial eigenvalue buckling mode shape was appropriately scaled and subsequently incorporated into the ideal geometry, ensuring that the maximum imperfection remained below the section thickness. This approach effectively integrated the initial imperfections into the FE model. Following this, a geometric nonlinear load-displacement analysis was conducted on the member exhibiting imperfections to ascertain its failure characteristics and load-bearing capacity.

3.4. Boundary conditions, contact, and loading

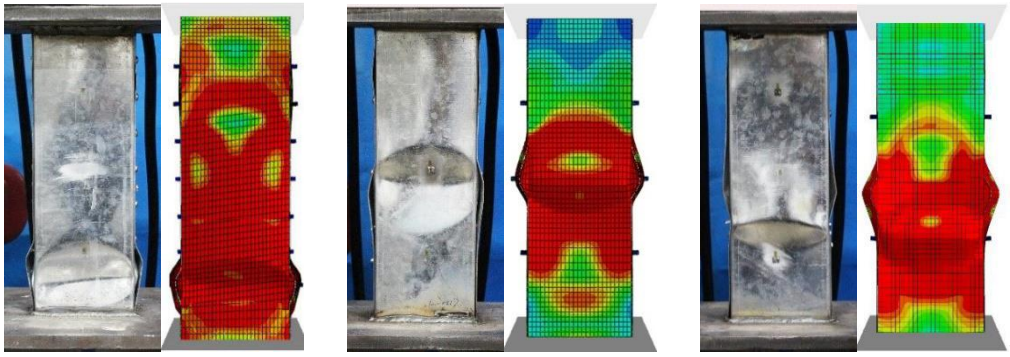
The end of the specimen was connected with the steel end-plate of the analytical rigid body through a “Tie”, as shown in Fig.12. The reference points RP1 and RP2 were established on the end-plate along the axial direction at each extremity of the column. The boundary conditions of fixed connections at both ends are achieved by regulating the degrees of freedom of the reference points RP1 and RP2, as illustrated in Fig.12. The six degrees of freedom associated with RP2, comprising three translational and three rotational degrees of freedom, were restricted. In contrast, five degrees of freedom for RP1 were constrained, with the exception of the directional freedom (*Uz*) along the length of the column, as illustrated in Fig. 12.

The interface between the screw and the screw hole is characterized by surface-to-surface contact, as illustrated in Fig.12. Furthermore, surface-to-surface contact was also established between the upper and lower flanges to prevent interpenetration of the contact surfaces of the two flanges, as depicted in Fig.12. Research findings presented in reference [40] suggest that the tangential friction force has a negligible effect on the assembled flanges; consequently, this frictional influence was disregarded in the contact settings. The FE analysis was conducted in two phases: eigenvalue analysis and nonlinear analysis. The eigenvalue analysis employed a concentrated load application method, while the nonlinear analysis utilized a displacement load application method. The loading was applied at the reference point RP1 in the axial direction along the column.

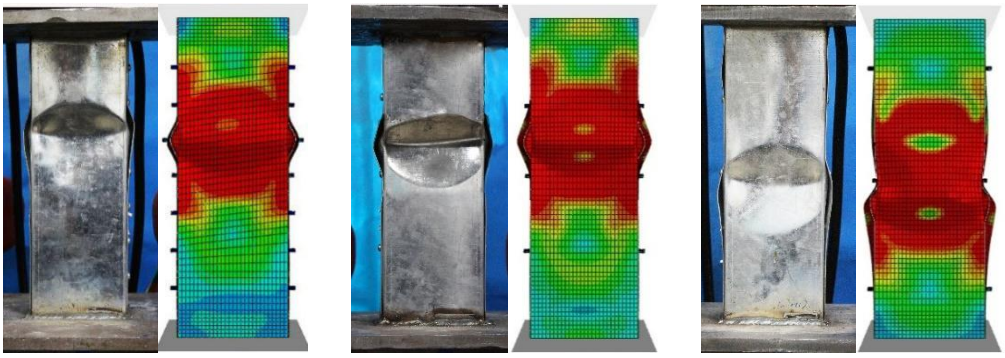
3.5. Numerical results and validation

3.5.1. Buckling and failure modes

The buckling modes, failure modes, and the failure location of the FE simulation were the same as those of the test results, as presented in Fig. 14. It showed that ripples were observed on the web of the C-section of the specimen before the local buckling failure of the flanges. And the peaks and troughs of the ripples were almost consistent with the position of the screw, as shown in Fig. 14. The verification results indicate that the FE model in this paper is accurate.



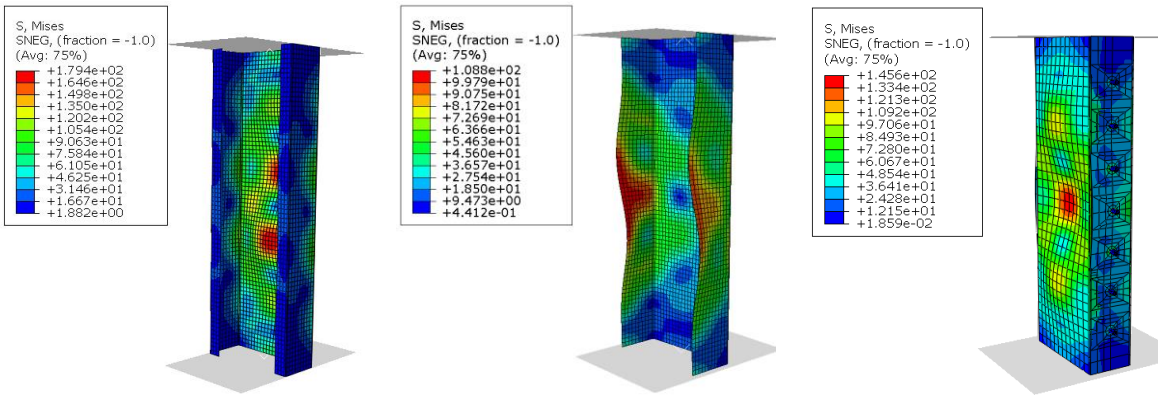
(a) B4-L120-45 (b) B4-L120-90 (c) B4-L120-150



(d) B4-L140-50 (e) B4-L140-100 (f) B4-L140-150

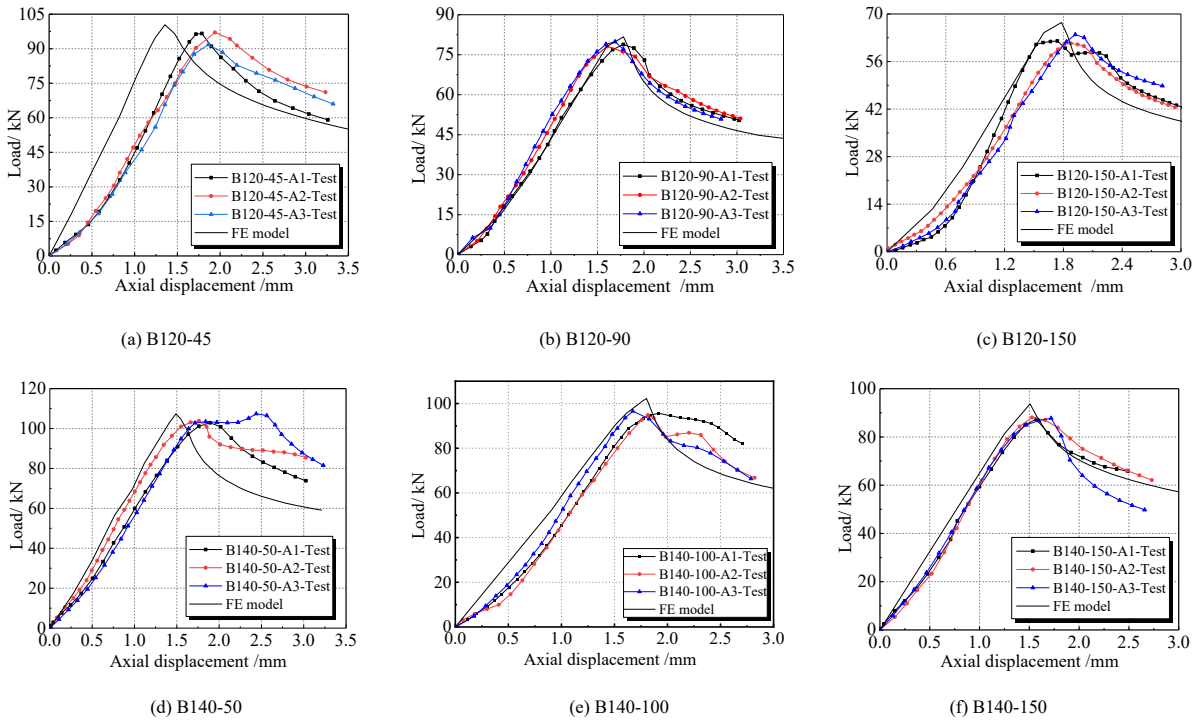
Fig. 14 Comparison of the failure modes

Therefore, the stress distribution plots from the FE analysis are used to explain the mechanism of stress redistribution and the interaction effect. Take the 120 series columns as an example. The local buckling stress distribution plots of the single-limb C-section, U-section, and built-up section are presented in Fig. 15(a) - 15(c) respectively. The internal stress of the specimen is relatively evenly distributed according to the overall stress condition before local buckling. When the local buckling begins to occur, the stress state in the buckling region changes significantly, and the uniformly distributed stress will transfer to the surrounding region without buckling. The maximum stress occurs in the web for single C-section column, as presented in Fig. 15(a). The maximum stress mainly occurs on both sides of the flange for single U-section column, as shown in Fig. 15(b). However, the maximum stress and the buckling position of the CFS built-up box-section column assembled by C- and U-section mainly occur in the middle of the web, as plotted in Fig. 15(c).



(a) C-section (b) U-section (c) Built-up section

Fig. 15 Stress distribution plots of the C-section, U-section, and Built-up section columns



(a) B120-45 (b) B120-90 (c) B120-150

(d) B140-50 (e) B140-100 (f) B140-150

Fig. 16 Comparison of the axial load-displacement

3.5.2. Bearing capacity and load-axial displacement curve

The load-bearing capacities obtained from the FE (P_{FE}) and test (P_t) are listed in Table 2. The mean value of P_{FE}/P_t is 1.07, with a standard deviation of 0.03. The FE simulation results were close to the experimental values, and the discreteness was small. Fig. 16 shows the load-axial displacement curves of the FE results and the experimental results. The slope of the curve of the FE specimen was basically the same as that of the test specimen before the specimen reached the ultimate bearing capacity. However, the test curve was relatively flat at the beginning of the curve in comparison. This is principally because there was a gap between the specimen and the device before loading. The trend of the load-axial displacement curve of the FE was basically consistent with that of the experimental specimen when the specimen was compacted. The peak point was also basically close. It is indicated that the accuracy and reliability of the FE model in this paper.

4. Discussion on the buckling mechanism

4.1. Built-up interaction effect on buckling strength

The different cross-sectional dimensions are listed in Table 4. Four series specimens are designed based on the height of the web (90mm、120mm、150mm and 200mm). The height-width ratio of the parameters varies from 1 to 13. The critical buckling stresses of the C- and U-section are analyzed by GBTUL software [41]. The ratio of $\sigma_{crL\text{-}U}$ to $\sigma_{crL\text{-}C}$ is analyzed to study the influence of the coordination between the two single-limb members on the built-up effect of the built-up columns. This paper could provide suggestions for the design of specimens in practical engineering. In addition, the ultimate capacities of the built-up columns with different height-width ratios are listed in Table 5. Taking 150 series of specimens as an example, the failure mode of the built-up column is shown in Fig 17.

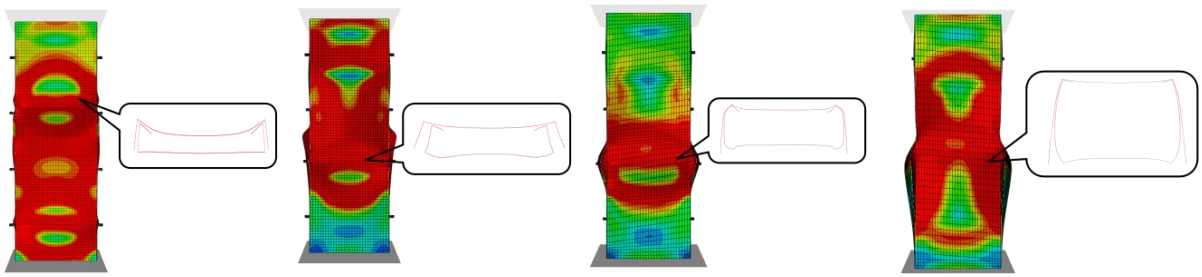
(1) From Table 4, it can be observed that the $\sigma_{crL\text{-}U}/\sigma_{crL\text{-}C}$ ratios of all specimens are on the rise for the width-to-thickness ratio $b/h \le 5$. Nevertheless, the $\sigma_{crL\text{-}U}/\sigma_{crL\text{-}C}$ ratios of 90 series specimens are on the decline for the width-to-thickness ratio $b/h<5$. The $\sigma_{crL\text{-}U}/\sigma_{crL\text{-}C}$ ratios of 120 series specimens are on the decline for the width-to-thickness ratio $6\le b/h\le 11$. However, the $\sigma_{crL\text{-}U}/\sigma_{crL\text{-}C}$ ratio begins to show an upward trend for the width-to-thickness ratio b/h≥12. The $\sigma_{crL\text{-}U}/\sigma_{crL\text{-}C}$ ratios of 150 series specimens are on the decline for the width-to-thickness ratio $6\le b/h\le 10$. However, the $\sigma_{crL\text{-}U}/\sigma_{crL\text{-}C}$ ratio begins to show an upward trend for the width-to-thickness ratio b/h≥11. The main reason may be that the flange width of the C-section is too narrow, and the lip length is much longer than the flange width, resulting in the C-section quickly reaching yield strength and buckling. Interestingly, the $\sigma_{crL\text{-}U}/\sigma_{crL\text{-}C}$ ratio of the 200 series specimens is unique. Like the observed specimens, the $\sigma_{crL\text{-}U}/\sigma_{crL\text{-}C}$ ratio is on the rise for $b/h\le 5$. However, the ratio $\sigma_{crL\text{-}U}/\sigma_{crL\text{-}C}$ changes irregularly with the increase of width-to-thickness ratio.

(2) From Table 5, the load-bearing capacity of the built-up column decreases by about 28.9% -37.1% for the column with a thickness of 1.0mm. While the load-bearing capacity of the built-up column decreases by about 31.9%~46.3% for the column with a thickness of 1.2mm. The ultimate capacity of each group of specimens decreases significantly with the increase of the height-width ratio. Except for individual specimens, the load-bearing capacity of the built-up column decreases by about 20% for every 2 times increase in the height-width ratio. Therefore, the height-width ratio of the cross-section is an important factor affecting the ultimate capacity of the CFS built-up box section column.

(3) The height-width ratio of the cross-section is also an important factor affecting the buckling mode of the CFS built-up column. In this study, local and distortional interactive buckling occurs in the CFSBBS columns with height-width ratios of 1 and 10, as presented in Fig. 17(a) and Fig. 17(d). The CFSBBS columns undergo local buckling with the height-width ratio of 2 and 5, as presented in Fig. 17(b) and Fig. 17(c).

Table 4
Critical local buckling stress of the C-section and U-section for CFSBBS columns

*h*b*d*t*	$\sigma_{crL\text{-}C}$	$\sigma_{crL\text{-}U}$	$\sigma_{crL\text{-}U}/\sigma_{crL\text{-}C}$		*h*b*d*t*	$\sigma_{crL\text{-}C}$	$\sigma_{crL\text{-}U}$	$\sigma_{crL\text{-}U}/\sigma_{crL\text{-}C}$	
90-90-15-1	41.6	5.16	0.12		150-150-15-1	22.17	3.11	0.14	
90-45-15-1	70.58	11.11	0.16	Rise	150-75-15-1	40.72	6.72	0.17	Rise
90-18-15-1	77.46	14.79	0.19		150-30-15-1	46.56	8.95	0.19	
90-15-15-1	79.34	13.68	0.17		150-25-15-1	47.91	8.37	0.17	
90-12.9-15-1	81.36	12.89	0.16		150-21.4-15-1	49.45	7.90	0.16	
90-11.3-15-1	83.38	12.20	0.15		150-18.8-15-1	50.97	7.52	0.15	
90-10-15-1	85.47	11.58	0.14	Decline	150-16.7-15-1	52.45	7.18	0.14	Decline
90-9-15-1	87.39	11.05	0.13		150-15-15-1	53.68	7.07	0.13	
90-8.2-15-1	89.13	10.58	0.12		150-13.6-15-1	12.88	6.66	0.52	
90-7.5-15-1	90.83	10.08	0.11		150-12.5-15-1	11.88	6.47	0.54	
90-6.9-15-1	92.40	9.36	0.10		150-11.5-15-1	10.99	6.28	0.57	
120-120-15-1	29.21	3.88	0.13		200-200-15-1	15.66	2.33	0.15	
120-60-15-1	53.13	8.38	0.16	Rise	200-100-15-1	28.44	5.06	0.18	Rise
120-24-15-1	60.98	11.15	0.18		200-40-15-1	31.62	6.73	0.21	
120-20-15-1	62.93	10.38	0.16		200-33.3-15-1	32.30	6.30	0.20	
120-17.1-15-1	65.21	9.79	0.15		200-28.6-15-1	12.30	5.96	0.48	
120-15-15-1	67.11	9.29	0.14		200-25-15-1	34.00	5.67	0.17	
120-13.3-15-1	69.19	8.87	0.13	Decline	200-22.2-15-1	34.83	5.43	0.16	Decline
120-12-15-1	70.96	8.51	0.12		200-20-15-1	35.46	5.32	0.15	
120-10.9-15-1	72.34	8.20	0.11		200-18.2-15-1	10.15	5.07	0.50	
120-10-15-1	13.77	7.93	0.58		200-16.7-15-1	10.15	4.93	0.49	
120-9.2-15-1	12.74	7.66	0.60		200-15.4-15-1	9.33	4.80	0.51	



(a) B150-15-1.2 (b) B150-30-1.2 (c) B150-75-1.2 (d) B150-150-1.2

Fig. 17 Failure modes of the B150-1.2series specimens

Table 5
Ultimate capacity of different height-width ratio of CFSBBS columns

Specimens	*h/b*	P_A/kN	Specimens	*h/b*	P_A/kN
B90-90-1	1	75.8	B90-90-1.2	1	109.1
B90-45-1	2	70.5	B90-45-1.2	2	102.7
B90-18-1	5	57.5	B90-18-1.2	5	76.6
B90-9.0-1	10	47.7	B90-9.0-1.2	10	58
B120-120-1	1	79.9	B120-120-1.2	1	112.7
B120-60-1	2	75.3	B120-60-1.2	2	105.8
B120-24-1	5	63	B120-24-1.2	5	85
B120-12-1	10	52.9	B120-12-1.2	10	63.5
B150-150-1	1	82	B150-150-1.2	1	114.1
B150-75-1	2	78.4	B150-75-1.2	2	107.5
B150-30-1	5	68.3	B150-30-1.2	5	90.7
B150-15-1	10	56.9	B150-15-1.2	10	74.8
B200-200-1	1	85.2	B200-200-1.2	1	118.3
B200-100-1	2	81.3	B200-100-1.2	2	111.9
B200-40-1	5	74.8	B200-40-1.2	5	99.4
B200-20-1	10	60.6	B200-20-1.2	10	80.6

4.2. Influence of screw spacing on the ultimate capacity

The significant difference between the specimen composed of two or more single limbs and the whole specimen is the fastener. This has also become a key factor affecting their carrying capacity. Therefore, in this study, three kinds of FE models (see Fig. 18) are developed to study the influence of screw spacing on the local buckling bearing capacity of the CFSBBS column. The sectional dimension of the specimen is shown in Table 6. The comparison results of the local buckling ultimate capacity are shown in Table 6 and Fig. 19. The ultimate capacities of the B type model are mostly higher than the A type model and smaller than C type model. However, it is interesting that the ultimate capacity of the four series of specimens in Table 6 does not decrease with the increase of screw spacing, but fluctuates repeatedly. The reason for the fluctuation in the local buckling ultimate capacity may be attributed to the screw spacing being related to the buckling half-wavelength of the specimen.

Table 6 indicates that the mean value of the P_A/P_B ratio is 0.972, accompanied by a standard deviation (SD) of 0.079. In contrast, the mean value of the P_C/P_B ratio is 1.224, with a standard deviation of 0.067. The analysis reveals a minimal dispersion associated with the increase in screw spacing. Fig. 9 illustrates that the curve representing the B type model closely resembles that of model A while diverging from model C. This observation suggests that variations in screw spacing exert a negligible influence on the local buckling ultimate capacity of CFSBBS short columns, and the strengthening effect on the cross-section is not pronounced. When the screw spacing is less than the buckling half-wavelength, the screws effectively constrain the number of buckling half-waves along the specimen's length, thereby enhancing its ultimate capacity. However, this constraint effect diminishes as screw spacing increases. The ultimate capacity experiences a slight increase when the screw spacing equals the buckling half-wavelength. Moreover, when the screw spacing exceeds the buckling half-wavelength, the constraining effect of the screws on the specimen weakens progressively with further increases in spacing, leading to a gradual decline in the specimen's ultimate capacity.

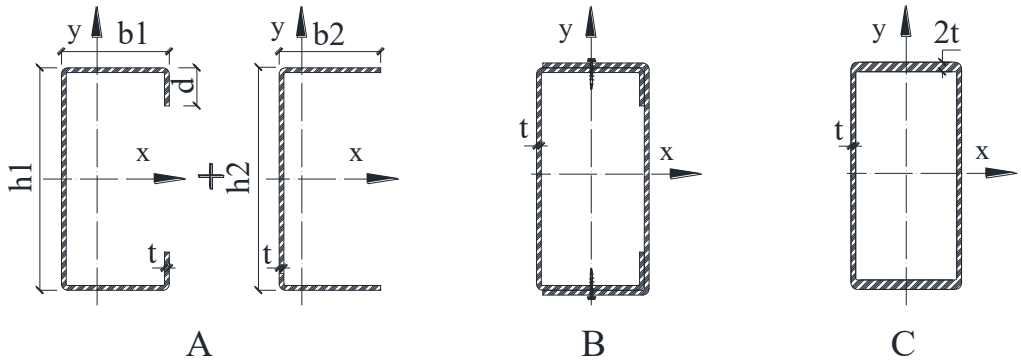


Fig. 18 Three calculation models

Table 6
Influence of screw spacing on the local buckling bearing capacity of CFS columns

Specimens	P_B/kN	P_A/kN	P_C/kN	P_A/P_B	P_C/P_B
B90-25-1	93.12			0.952	1.187
B90-50-2	92.37			0.960	1.197
B90-70-3	93.11	88.67	110.53	0.952	1.187
B90-100-4	91.88			0.965	1.203
B90-150-5	91.90			0.965	1.203
B120-25-6	110.97			0.925	1.272
B120-55-7	106.07			0.968	1.331
B120-91-8	109.68	102.68	141.16	0.936	1.287
B120-120-9	105.22			0.976	1.342
B120-150-10	105.51			0.973	1.338
B120-180-11	106.46			0.965	1.326
B150-25-12	111.77			0.941	1.129
B150-55-13	107.99			0.974	1.169
B150-85-14	105.53			0.997	1.196
B150-117-15	110.69	105.21	126.23	0.950	1.140
B150-150-16	106.87			0.984	1.181
B150-180-17	106.95			0.984	1.180
B150-210-18	107.65			0.977	1.173
B200-25-19	115.78			0.971	1.147
B200-75-20	114.30			0.984	1.162
B200-125-21	113.96			0.986	1.165
B200-156-22	114.68	112.42	132.80	0.980	1.158
B200-180-23	113.64			0.992	1.169
B200-210-23	113.54			0.990	1.170
B200-240-24	113.14			0.994	1.174
Mean				0.972	1.224
SD				0.079	0.067

Note：P_A、P_B、P_C represent the ultimate capacity of finite element for A, B and C models, respectively.

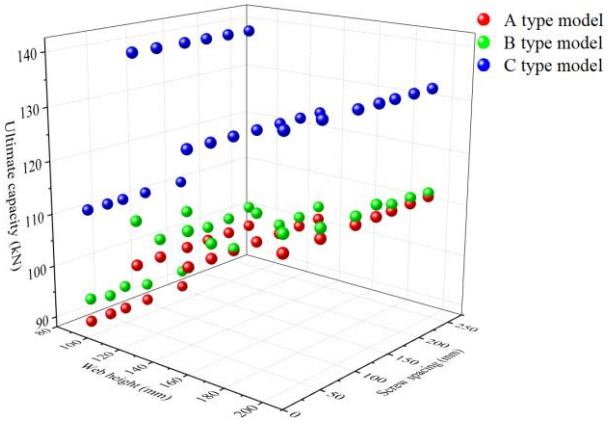


Fig. 19 Influence of screw spacing on the bearing capacity of CFS columns

5. Conclusion and discussion

This study examines the local buckling mechanism through both experimental and numerical simulations, focusing on various aspects such as buckling behavior, buckling modes, load-bearing capacity, post-buckling strength, and the interaction effects of the CFSBBS columns. The influence of screw spacing on the buckling mechanism was thoroughly analyzed through comprehensive parametric studies. The following significant conclusions have been drawn:

(1) The local buckling patterns of the CFSBBS column were clarified. There are 5 types of buckling modes (see Fig.11(d)-(h)) for the same specimen with different cross-sections. This deformation process reveals the mechanism of local buckling instability of the CFSBBS columns.

(2) The smaller the ratio $\sigma_{crL\text{-}U}$ /$\sigma_{crL\text{-}C}$, the greater the deformation coordination effect of the C-section on the U-section, and the more likely the built-up part of the CFSBBS column is to undergo coordinated deformation, and the more obvious the built-up effect is.

(3) Screw spacing can not make a large gap in the bearing capacity of the CFS built-up box section columns. However, the buckling mode of the CFS built-up column will change with the increase of the screw spacing. In addition, almost all of the built-up plates are coordinated buckling deformation, which also lays the foundation for the theoretical study of the CFSBBS column subjected to local buckling by the author's team. The author will carry out experimental and theoretical research on the buckling mechanism of different built-up sections.

(4) When the screw spacing is less than the half-wavelength (λ_c), the local buckling ultimate capacity of the CFS built-up box section column decreases with the increase of the screw spacing. When the screw spacing is equal to the λ_c, the ultimate capacity does not increase significantly. While the ultimate capacity shows a downward trend when the screw spacing is greater than the λ_c.

(5) Appropriate screw spacing can ensure that the connection between adjacent components can adapt to this buckling and avoid local stress concentration leading to failure. In the processing stage of CFS members, the use of high-precision equipment can ensure the dimensional accuracy and shape regularity of the steel and reduce the defects caused by the quality problems of the material itself. The research results are beneficial to the popularization and application of CFSBBS column in the field of residential and industrial buildings.

Declaration of competing interest

The authors declare that they have no known competing financial interests or personal relationships that could have appeared to influence the work reported in this paper.

Acknowledgments

The authors sincerely appreciate the financial support provided by the Key R&D and promotion projects in Henan Province (No.242102321151) and (No.242102321152), Key Scientific Research Projects of Colleges and Universities in Henan province (23A560011) and (22A560013), Water conservancy project innovative science and technology team cultivation plan (2023XK100100086).

References

[1] Selvaraj S, Madhavan M. Structural Behaviour of Cold-Formed Steel Built-Up Closed Cross-section Columns - Assessing the Influence of Parameters and Design Methods. Engineering Structures 2023; 294:116600.
[2] Nie SF, Eatherton MR, Han Y, et al. Investigation of built-up box columns composed of four cold-formed steel channels. Thin-Walled Struct 2022; 175:109258.
[3] Deepak MS, Ananthi GBG. Local buckling behaviour and capacities of Cold-Formed Steel Double-I-Box stub and short column sections. Structures 2021; 34:1761-1784.
[4] Huynh MT, Pham CH, Hancock GJ. Experimental behaviour and modelling of screwed connections of high strength sheet steels in shear. Thin-Walled Struct 2020; 146:106357.
[5] Kherbouche S, Megnounif A. Numerical study and design of thin walled cold formed steel built-up open and closed section columns. Engineering Structures 2019; 179:670-682.
[6] Wang LP, Young B. Behaviour and design of cold-formed steel built-up section beams with different screw arrangements. Thin-Walled Struct 2018;131:16–32.
[7] Li YQ, Li YL, Wang S, Shen ZY. Ultimate load-carrying capacity of cold-formed thin-walled columns with built-up box and I section under axial compression. Thin-Walled Structures, 2014, 79:202–217.
[8] Yang JJ, Xu L, Shi Y, Wang WY. Experimental and analytical study of flexural buckling of cold-formed steel quadruple-limb built-up box columns. Journal of Structural Engineering, 2022, 148(1):04021228.
[9] Zhang L, Zhou TH, Sang LR, Wang YZ, Wang SB. Experiments on local-distortional interaction buckling of cold-formed steel three-limbed built-up open-section columns. Thin-Walled Structures, 2023, 182:110239.
[10] Li YC, Zhou TH, Han AH, Li WH, Xu Y. Failure mechanism and reliability prediction of CFS built-up columns considering distortional buckling. Structures, 2024, 69:107337.
[11] Li YC, Li RB, Zhou TH, Han AH, Li WH. Mechanics of cold-formed steel built-up box section columns in local buckling modes. Structures, 2025, 71:107957.
[12] Timoshenko SP. Theory of Elastic Stability, 2nd ed., Mcgraw-Hill, New York. 1961.
[13] Bleich F. Buckling Strength of Metal Structures. Mcgraw-Hill, 1952.
[14] Szymczak C, Kujawa M. On local buckling of cold-formed channel members. Thin-Walled Structures, 2016, 106:93-101.
[15] Ragheb WF. Local buckling of welded steel I-beams considering flange–web interaction. Thin-Walled Structures, 2015, 97:241-249.
[16] Li YC, Li RB, Zhou TH, et al. Novel design method of screwed connections of cold-formed steel built-up plates. Structures, 2023, 55:2433–2444.
[17] Roy K, Ting TCH, et al. Effect of thickness on the behaviour of axially loaded backto-back cold-formed steel built-up channel sections-Experimental and numerical investigation. Structures, 2018, 16:327–46.
[18] Pham DK, Pham CH, Pham SH, et al. Experimental investigation of high strength cold-formed channel sections in shear with rectangular and slotted web openings. J Constr Steel Res, 2020;165:105889.
[19] Li YC, Zhou TH, Zhang L, et al. Distortional buckling behavior of cold-formed steel built-up closed section columns. Thin-Walled Struc, 2021;166:108069.
[20] Zhou TH, Li YC, Ren LJ, et al. Research on the elastic buckling of composite webs in cold-formed steel back-to-back built-up columns - Part I: Experimental and numerical investigation. Structures, 2021;30:115–133.
[21] Fratamico DC, Torabian S, Zhao Xi, Rasmussen KJR, Schafer BW. Experimental study on the composite action in sheathed and bare built-up cold-formed steel columns. Thin-Walled Struct, 2018, 127:290-305.
[22] Chen B, Roy K, Uzzaman A, Raftery G, Lim JBP. Axial strength of back-to-back cold-formed steel channels with edge-stiffened holes, un-stiffened holes and plain webs. J Constr Steel Res, 2020, 174:106313.
[23] Ting TCH, Roy K, Lau HH, et al. Effect of screw spacing on behavior of axially loaded back-to-back cold-formed steel built-up channel sections. Adv Struct Eng 2018, 21(3):474–87.
[24] Roy K, Ting TCH, Lau HH, et al. Nonlinear behaviour of back-to-back gapped builtup cold-formed steel channel sections under compression. J Constr Steel Res, 2018, 147:257–76.
[25] Wang L, Young B. Behaviour and design of cold-formed steel built-up section beams with different screw arrangements. Thin-Walled Struct, 2018, 131:16–32.
[26] Roy K, Lau HH, Ting TCH, et al. Experiments and finite element modelling of screw pattern of self-drilling screw connections for high strength cold-formed steel. ThinWalled Struc, 2019, 145:106393.
[27] Lu Y, Zhou TH, Li WC, et al. Experimental investigation and a novel direct strength method for cold-formed built-up I-section columns. Thin-Walled Structures, 2017, 112:125–139.
[28] Zhou TH, Li YC, Wu HH, et al. Superposition method for bearing capacity of cold-formed thin-walled steel built-up box-section short columns. Journal of Hunan University, China, 2020, 47(11):46-55.
[29] Li YC, Zhou TH, Ding JH, et al. Investigation on distortion buckling behavior of cold-formed thin-walled steel built-up box-section columns. Journal of Hunan University, China, 2021, 48(11):91-100.
[30] Reyes W, Guzmán A. Evaluation of the slenderness ratio in built-up cold-formed box sections. Journal of Constructional Steel Research, 2011, 67(6): 929-935.
[31] Selvaraj S, Madhavan M. Design of cold-formed steel built-up closed section columns using direct strength method. Thin-Walled Struct, 2022, 171:108746.
[32] Abbasi M, Rasmussen KJR, Kheari M, et al. Experimental investigation of the sectional buckling of built-up cold-formed steel columns. J Constr Steel Res, 2023, 203:107803.
[33] Qiao WT, Wang YH, Li RF, et al. Research on axial bearing capacity of cold-formed thin-walled steel built-up column with 12-limb-section. Steel Compos. Struct, 2023, 47(3):437–450.
[34] Lu Y, Zhou TH, Li WC, et al. The critical local buckling load and ultimate strength of cold-formed thin-walled C-sections under axial compression. Journal of Harbin Institute of Technology, 2017, 49(6):72-76. (In Chinese)
[35] Schafer BW, CUFSM4.05—finite strip buckling analysis of thin-walled members. Department of Civil Engineering, Johns Hopkins University, Baltimore, U.S.A, 2012.
[36] AISI S100, North American Specification for the Design of Cold-Formed Steel Structural Members, American Iron and Steel Institute, Washington, DC, 2016.
[37] Ziemian RD. Guide to Stability Design Criteria for Metal Structures. Sixth edition, Hoboken: John Wiley & Sons, 2010.
[38] ABAQUS, ABAQUS Analysis user's Manual, Version 6.21, Dassault Syst`emes Simulia Corp, Providence, RI, USA, 2021.
[39] Schafer BW, Li Z, Moen CD. Computational modeling of cold-formed steel. Thin-Walled Structures, 2010, 48(10):752-762.
[40] Zhang JH, Young B. Numerical investigation and design of cold-formed steel built-up open section columns with longitudinal stiffeners. Thin-Walled Structures, 2015, 89(4):178-191.
[41] Bebiano R, Pina P, Silvestre N, et al. GBTUL — buckling and vibration analysis of thin-walled members. Lisbon, Technical University of Lisbon, 2008.